DESY-99-107
August 1999

ISSN 0418-9833

Measurement of Neutral and Charged Current Cross-Sections in Positron-Proton Collisions at Large Momentum Transfer

H1 Collaboration

Abstract

The inclusive single and double differential cross-sections for neutral and charged current processes with four-momentum transfer squared Q^2 between 150 and $30\,000$ GeV^2 and with Bjorken x between 0.0032 and 0.65 are measured in e^+p collisions. The data were taken with the H1 detector at HERA between 1994 and 1997, and they correspond to an integrated luminosity of 35.6 pb^{-1}. The Q^2 evolution of the parton densities of the proton is tested, yielding no significant deviation from the prediction of perturbative QCD. The proton structure function $F_2(x, Q^2)$ is determined. An extraction of the u and d quark distributions at high x is presented. At high Q^2 electroweak effects of the heavy bosons Z° and W are observed and found to be consistent with Standard Model expectation.

Submitted to the European Journal of Physics

C. Adloff[33], V. Andreev[24], B. Andrieu[27], V. Arkadov[34], A. Astvatsatourov[34], I. Ayyaz[28], A. Babaev[23], J. Bähr[34], P. Baranov[24], E. Barrelet[28], W. Bartel[10], U. Bassler[28], P. Bate[21], A. Beglarian[10,39], O. Behnke[10], H.-J. Behrend[10], C. Beier[14], A. Belousov[24], Ch. Berger[1], G. Bernardi[28], T. Berndt[14], G. Bertrand-Coremans[4], P. Biddulph[21], J.C. Bizot[26], V. Boudry[27], W. Braunschweig[1], V. Brisson[26], H.-B. Bröker[2], D.P. Brown[21], W. Brückner[12], P. Bruel[27], D. Bruncko[16], J. Bürger[10], F.W. Büsser[11], A. Bunyatyan[12,39], S. Burke[17], A. Burrage[18], G. Buschhorn[25], D. Calvet[22], A.J. Campbell[10], T. Carli[25], E. Chabert[22], M. Charlet[4], D. Clarke[5], B. Clerbaux[4], J.G. Contreras[7,42], C. Cormack[18], J.A. Coughlan[5], M.-C. Cousinou[22], B.E. Cox[21], G. Cozzika[9], J. Cvach[29], J.B. Dainton[18], W.D. Dau[15], K. Daum[33,38], M. David[9,†] M. Davidsson[20], A. De Roeck[10], E.A. De Wolf[4], B. Delcourt[26], R. Demirchyan[10,40], C. Diaconu[22], M. Dirkmann[7], P. Dixon[19], V. Dodonov[12], K.T. Donovan[19], J.D. Dowell[3], A. Droutskoi[23], J. Ebert[33], G. Eckerlin[10], D. Eckstein[34], V. Efremenko[23], S. Egli[36], R. Eichler[35], F. Eisele[13], E. Eisenhandler[19], E. Elsen[10], M. Enzenberger[25], M. Erdmann[13,41,f], A.B. Fahr[11], P.J.W. Faulkner[3], L. Favart[4], A. Fedotov[23], R. Felst[10], J. Feltesse[9], J. Ferencei[10], F. Ferrarotto[31], S. Ferron[27], M. Fleischer[10], G. Flügge[2], A. Fomenko[24], J. Formánek[30], J.M. Foster[21], G. Franke[10], E. Gabathuler[18], K. Gabathuler[32], F. Gaede[25], J. Garvey[3], J. Gassner[32], J. Gayler[10], R. Gerhards[10], S. Ghazaryan[10,39], A. Glazov[34], L. Goerlich[6], N. Gogitidze[24], M. Goldberg[28], I. Gorelov[23], C. Grab[35], H. Grässler[2], T. Greenshaw[18], R.K. Griffiths[19], G. Grindhammer[25], T. Hadig[1], D. Haidt[10], L. Hajduk[6], M. Hampel[1], V. Haustein[33], W.J. Haynes[5], B. Heinemann[10], G. Heinzelmann[11], R.C.W. Henderson[17], S. Hengstmann[36], H. Henschel[34], R. Heremans[4], G. Herrera[7,43,l], I. Herynek[29], K. Hewitt[3], M. Hilgers[35], K.H. Hiller[34], C.D. Hilton[21], J. Hladký[29], P. Höting[2], D. Hoffmann[10], R. Horisberger[32], S. Hurling[10], M. Ibbotson[21], Ç. İşsever[7], M. Jacquet[26], M. Jaffre[26], L. Janauschek[25], D.M. Jansen[12], L. Jönsson[20], D.P. Johnson[4], M. Jones[18], H. Jung[20], H.K. Kästli[35], M. Kander[10], D. Kant[19], M. Kapichine[8], M. Karlsson[20], O. Karschnick[11], O. Kaufmann[13], M. Kausch[10], F. Keil[14], N. Keller[13], I.R. Kenyon[3], S. Kermiche[22], C. Kiesling[25], M. Klein[34], C. Kleinwort[10], G. Knies[10], J.H. Köhne[25], H. Kolanoski[37], S.D. Kolya[21], V. Korbel[10], P. Kostka[34], S.K. Kotelnikov[24], T. Krämerkämper[7], M.W. Krasny[28], H. Krehbiel[10], D. Krücker[25], K. Krüger[10], A. Küpper[33], H. Küster[2], M. Kuhlen[25], T. Kurča[34], W. Lachnit[10], R. Lahmann[10], D. Lamb[3], M.P.J. Landon[19], W. Lange[34], U. Langenegger[35], A. Lebedev[24], F. Lehner[10], V. Lemaitre[10], R. Lemrani[10], V. Lendermann[7], S. Levonian[10], M. Lindstroem[20], G. Lobo[26], E. Lobodzinska[6,40], V. Lubimov[23], S. Lüders[35], D. Lüke[7,10], L. Lytkin[12], N. Magnussen[33], H. Mahlke-Krüger[10], N. Malden[21], E. Malinovski[24], I. Malinovski[24], R. Maraček[25], P. Marage[4], J. Marks[13], R. Marshall[21], H.-U. Martyn[1], J. Martyniak[6], S.J. Maxfield[18], T.R. McMahon[18], A. Mehta[5], K. Meier[14], P. Merkel[10], F. Metlica[12], A. Meyer[10], H. Meyer[33], J. Meyer[10], P.-O. Meyer[2], S. Mikocki[6], D. Milstead[10], R. Mohr[25], S. Mohrdieck[11], M.N. Mondragon[7], F. Moreau[27], A. Morozov[8], J.V. Morris[5], D. Müller[36], K. Müller[13], P. Murín[16,44], V. Nagovizin[23], B. Naroska[11], J. Naumann[7], Th. Naumann[34], I. Négri[22], P.R. Newman[3], H.K. Nguyen[28], T.C. Nicholls[10], F. Niebergall[11], C. Niebuhr[10], Ch. Niedzballa[1], H. Niggli[35], O. Nix[14], G. Nowak[6], T. Nunnemann[12], H. Oberlack[25], J.E. Olsson[10], D. Ozerov[23], P. Palmen[2], V. Panassik[8], C. Pascaud[26], S. Passaggio[35], G.D. Patel[18], H. Pawletta[2], E. Perez[9], J.P. Phillips[18], A. Pieuchot[10], D. Pitzl[35], R. Pöschl[7], I. Potashnikova[12], B. Povh[12], K. Rabbertz[1], G. Rädel[9], J. Rauschenberger[11], P. Reimer[29], B. Reisert[25], D. Reyna[10], S. Riess[11], E. Rizvi[3], P. Robmann[36], R. Roosen[4], K. Rosenbauer[1], A. Rostovtsev[23,10], C. Royon[9], S. Rusakov[24], K. Rybicki[6], D.P.C. Sankey[5], P. Schacht[25], J. Scheins[1], F.-P. Schilling[13], S. Schleif[14], P. Schleper[13], D. Schmidt[33], D. Schmidt[10], L. Schoeffel[9], T. Schörner[25], V. Schröder[10], H.-C. Schultz-Coulon[10], F. Sefkow[36], V. Shekelyan[25], I. Sheviakov[24], L.N. Shtarkov[24], G. Siegmon[15], Y. Sirois[27], T. Sloan[17], P. Smirnov[24], M. Smith[18], V. Solochenko[23], Y. Soloviev[24], V. Spaskov[8], A. Specka[27], H. Spitzer[11],

F. Squinabol[26], R. Stamen[7], J. Steinhart[11], B. Stella[31], A. Stellberger[14], J. Stiewe[14], U. Straumann[13], W. Struczinski[2], J.P. Sutton[3], M. Swart[14], S. Tapprogge[14], M. Taševský[29], V. Tchernyshov[23], S. Tchetchelnitski[23], G. Thompson[19], P.D. Thompson[3], N. Tobien[10], R. Todenhagen[12], D. Traynor[19], P. Truöl[36], G. Tsipolitis[35], J. Turnau[6], E. Tzamariudaki[25], S. Udluft[25], A. Usik[24], S. Valkár[30], A. Valkárová[30], C. Vallée[22], P. Van Mechelen[4], Y. Vazdik[24], G. Villet[9], K. Wacker[7], R. Wallny[13], T. Walter[36], B. Waugh[21], G. Weber[11], M. Weber[14], D. Wegener[7], A. Wegner[11], T. Wengler[13], M. Werner[13], L.R. West[3], G. White[17], S. Wiesand[33], T. Wilksen[10], M. Winde[34], G.-G. Winter[10], Ch. Wissing[7], C. Wittek[11], M. Wobisch[2], H. Wollatz[10], E. Wünsch[10], J. Žáček[30], J. Zálešák[30], Z. Zhang[26], A. Zhokin[23], P. Zini[28], F. Zomer[26], J. Zsembery[9] and M. zur Nedden[10]

[1] I. Physikalisches Institut der RWTH, Aachen, Germany[a]
[2] III. Physikalisches Institut der RWTH, Aachen, Germany[a]
[3] School of Physics and Space Research, University of Birmingham, Birmingham, UK[b]
[4] Inter-University Institute for High Energies ULB-VUB, Brussels; Universitaire Instelling Antwerpen, Wilrijk; Belgium[c]
[5] Rutherford Appleton Laboratory, Chilton, Didcot, UK[b]
[6] Institute for Nuclear Physics, Cracow, Poland[d]
[7] Institut für Physik, Universität Dortmund, Dortmund, Germany[a]
[8] Joint Institute for Nuclear Research, Dubna, Russia
[9] DSM/DAPNIA, CEA/Saclay, Gif-sur-Yvette, France
[10] DESY, Hamburg, Germany[a]
[11] II. Institut für Experimentalphysik, Universität Hamburg, Hamburg, Germany[a]
[12] Max-Planck-Institut für Kernphysik, Heidelberg, Germany[a]
[13] Physikalisches Institut, Universität Heidelberg, Heidelberg, Germany[a]
[14] Institut für Hochenergiephysik, Universität Heidelberg, Heidelberg, Germany[a]
[15] Institut für experimentelle und angewandte Physik, Universität Kiel, Kiel, Germany[a]
[16] Institute of Experimental Physics, Slovak Academy of Sciences, Košice, Slovak Republic[f,j]
[17] School of Physics and Chemistry, University of Lancaster, Lancaster, UK[b]
[18] Department of Physics, University of Liverpool, Liverpool, UK[b]
[19] Queen Mary and Westfield College, London, UK[b]
[20] Physics Department, University of Lund, Lund, Sweden[g]
[21] Department of Physics and Astronomy, University of Manchester, Manchester, UK[b]
[22] CPPM, Université d'Aix-Marseille II, IN2P3-CNRS, Marseille, France
[23] Institute for Theoretical and Experimental Physics, Moscow, Russia
[24] Lebedev Physical Institute, Moscow, Russia[f,k]
[25] Max-Planck-Institut für Physik, München, Germany[a]
[26] LAL, Université de Paris-Sud, IN2P3-CNRS, Orsay, France
[27] LPNHE, École Polytechnique, IN2P3-CNRS, Palaiseau, France
[28] LPNHE, Universités Paris VI and VII, IN2P3-CNRS, Paris, France
[29] Institute of Physics, Academy of Sciences of the Czech Republic, Praha, Czech Republic[f,h]
[30] Nuclear Center, Charles University, Praha, Czech Republic[f,h]
[31] INFN Roma 1 and Dipartimento di Fisica, Università Roma 3, Roma, Italy
[32] Paul Scherrer Institut, Villigen, Switzerland
[33] Fachbereich Physik, Bergische Universität Gesamthochschule Wuppertal, Wuppertal, Germany[a]

[34] DESY, Zeuthen, Germany[a]
[35] Institut für Teilchenphysik, ETH, Zürich, Switzerland[i]
[36] Physik-Institut der Universität Zürich, Zürich, Switzerland[i]

[37] Present address: Institut für Physik, Humboldt-Universität, Berlin, Germany[a]
[38] Also at Rechenzentrum, Bergische Universität Gesamthochschule Wuppertal, Wuppertal, Germany[a]
[39] Visitor from Yerevan Physics Institute, Armenia
[40] Foundation for Polish Science fellow
[41] Also at Institut für Experimentelle Kernphysik, Universität Karlsruhe, Karlsruhe, Germany
[42] Also at Dept. Fis. Ap. CINVESTAV, Mérida, Yucatán, México
[43] On leave from CINVESTAV, México
[44] Also at University of P.J. Šafárik, Košice, Slovak Republic

† Deceased

[a] Supported by the Bundesministerium für Bildung, Wissenschaft, Forschung und Technologie, FRG, under contract numbers 7AC17P, 7AC47P, 7DO55P, 7HH17I, 7HH27P, 7HD17P, 7HD27P, 7KI17I, 6MP17I and 7WT87P
[b] Supported by the UK Particle Physics and Astronomy Research Council, and formerly by the UK Science and Engineering Research Council
[c] Supported by FNRS-FWO, IISN-IIKW
[d] Partially supported by the Polish State Committee for Scientific Research, grant no. 115/E-343/SPUB/P03/002/97 and grant no. 2P03B 055 13
[e] Supported in part by US DOE grant DE F603 91ER40674
[f] Supported by the Deutsche Forschungsgemeinschaft
[g] Supported by the Swedish Natural Science Research Council
[h] Supported by GA ČR grant no. 202/96/0214, GA AV ČR grant no. A1010821 and GA UK grant no. 177
[i] Supported by the Swiss National Science Foundation
[j] Supported by VEGA SR grant no. 2/5167/98
[k] Supported by Russian Foundation for Basic Research grant no. 96-02-00019
[l] Supported by the Alexander von Humboldt Foundation

1 Introduction

The deep-inelastic scattering (DIS) of leptons off nucleons has played a fundamental role in understanding the structure of matter and in the foundation of the Standard Model as the theory of strong and electroweak interactions. The first DIS measurements revealed the existence of partons in the proton [1] and opened the way to the development of Quantum Chromodynamics (QCD) as the theory of strong interactions. The establishment of electroweak theory followed the observation of neutral current neutrino scattering [2]. Subsequent (fixed target) DIS experiments [3, 4, 5] have helped to constrain the electroweak parameters of the Standard Model and the partonic structure of the proton.

At HERA, the first electron-proton (ep) collider ever built, the study of DIS has been further pursued since 1992. There are two contributions to DIS, both of which can be measured at HERA, neutral current (NC) interactions, $ep \to eX$, and charged current (CC) interactions, $ep \to \nu X$. In the Standard Model a photon (γ) or a Z° boson is exchanged in a NC interaction, and a $W^\pm$ boson is exchanged in a CC interaction. DIS can be described by the four-momentum transfer squared Q^2, Bjorken x and inelasticity y defined as

$$Q^2 = -q^2 \equiv -(k - k')^2 \qquad x = \frac{Q^2}{2p \cdot q} \qquad y = \frac{p \cdot q}{p \cdot k}\,, \tag{1}$$

with $k(k')$ and p being the four-momentum of the incident (scattered) lepton and proton. The centre-of-mass energy $\sqrt{s}$ of the ep interaction is given by $s \equiv (p + k)^2 = Q^2/xy$ when neglecting the proton and positron masses.

The kinematic range of DIS measurements is extended to $Q^2 = 30\,000\ \mathrm{GeV}^2$ at high x with this analysis. The fixed target experiments covered the kinematic plane up to $Q^2 = 250\ \mathrm{GeV}^2$ and down to $x \approx 10^{-2}$. Previous results by the HERA experiments, H1 and ZEUS, extended to higher values of $Q^2 = 5000\ \mathrm{GeV}^2$ and to lower values of $x \approx\ 10^{-5}$ at low Q^2 [6, 7]. The extensions in kinematic domain are made possible at HERA by the positron and proton beam energies of $E_e = 27.6\ \mathrm{GeV}$ and $E_p = 820\ \mathrm{GeV}$ and consequently large $\sqrt{s} \approx 300\ \mathrm{GeV}$.

For NC interactions at low x, the measurements of the proton structure function F_2 revealed [8, 9] a strong rise with decreasing x, which can be understood within perturbative QCD in the form of Next-to-Leading Order (NLO) DGLAP [10] evolution equations. The kinematic reach in x at high Q^2 allowed cross-sections which are directly related to the valence quark distributions of the proton to be measured, albeit with limited precision. For CC interactions measurements of e^-p and e^+p single differential cross-sections extended the results obtained in fixed target neutrino and antineutrino scattering to higher Q^2 [11, 12]. The measurements were used to determine the W propagator mass M_W.

In this paper measurements of the NC and CC cross-sections at high Q^2 are presented. The results are obtained using e^+p data taken between 1994 and 1997. The integrated luminosity of $35.6\ \mathrm{pb}^{-1}$ is more than a factor of 10 greater than for previously published measurements of NC and CC cross-sections by H1 [6, 11]. The increase in integrated luminosity enables both the influence of the Z° boson in NC interactions and the helicity structure of the CC interaction to be tested in the high Q^2 domain. The behaviour of the NC and CC cross-sections at the highest

Q^2 is of particular interest following the observation by H1 and ZEUS [13, 14] of an excess over Standard Model expectation of NC events at Q^2 greater than $15\,000\ \mathrm{GeV}^2$ using the e^+p data taken between 1994 and 1996. A detailed analysis of the significance of this excess using the complete e^+p data set used here is presented in [15]. Recently measurements of the NC and CC cross-sections at high Q^2 have been reported by the ZEUS experiment [16, 17].

This paper consists of five sections. In section 2 the experimental technique used for the measurements is presented. In section 3 the procedures used for the cross-section measurement, and the QCD analysis which is used subsequently to interpret the data, are described. In section 4 the cross-section measurements and their interpretation are presented. The paper is summarized in section 5.

2 Experimental Technique

2.1 Kinematic Reconstruction

The measurement of the differential DIS cross-sections relies on the precise determination of the kinematic variables of each event. Different reconstruction methods are used for CC and NC interactions.

For CC interactions the kinematic variables can only be reconstructed using the hadronic final state because the neutrino (ν) is not detected. To characterize the hadronic final state, it is convenient to introduce the quantity Σ, the transverse momentum $P_{T,h}$, and the inclusive hadronic angle γ_h defined by

$$\Sigma = \sum_i (E_i - p_{z,i}) \qquad P_{T,h} = \sqrt{(\sum_i p_{x,i})^2 + (\sum_i p_{y,i})^2} \qquad \tan\frac{\gamma_h}{2} = \frac{\Sigma}{P_{T,h}}\,. \tag{2}$$

Here E_i and $p_{z,i}$ are the energy and longitudinal momentum component of a particle i, and $p_{x,i}$, $p_{y,i}$ are its momentum components in the plane orthogonal to the z-axis[1]. The summation is over all hadronic final state particles, whose rest masses are neglected[2]. The kinematic variables are then obtained from [18]

$$y_h = \frac{\Sigma}{2\,E_e} \qquad Q^2_h = \frac{P^2_{T,h}}{1-y_h} \qquad x_h = \frac{Q^2_h}{s\,y_h}\,. \tag{3}$$

This "hadron method" (h method) gives moderate precision in the reconstruction of the kinematic variables because of particle losses in the beam-pipe and because of fluctuations of the detector response to hadronic final state particles. It is thus used only for the CC interactions.

For NC interactions different methods of determining the kinematic variables are possible since there is redundant information from the simultaneous reconstruction of the scattered

[1]The forward direction and the positive z-axis are defined at HERA as the proton beam direction.

[2]The $p_{x,h}$ and $p_{y,h}$ components of the hadronic transverse momentum vector $\vec{P}_{T,h}$ are defined using the same summation over $p_{x,i}$ and $p_{y,i}$ respectively.

positron and of the hadronic final state. The choice of the method determines the corrections due to resolution and radiative effects, and the size of the systematic errors. In the "electron method" (e method) the energy E'_e and the polar angle θ_e of the scattered positron are used to determine the variables

$$y_e = 1 - \frac{E'_e(1-\cos\theta_e)}{2\,E_e} \qquad Q^2_e = \frac{P^2_{T,e}}{1-y_e} \qquad x_e = \frac{Q^2_e}{s\,y_e} \tag{4}$$

with $P_{T,e} = E'_e \sin\theta_e$. The e method has excellent resolution in Q^2 and in x at large y. The Σ method [19] makes use of the positron and the hadronic final state variables. It has a better resolution in x at low y and is less sensitive to radiative effects since

$$y_\Sigma = \frac{\Sigma}{E-p_z} \qquad \text{with} \qquad E - p_z = \Sigma + E'_e(1-\cos\theta_e) \tag{5}$$

does not depend on the energy of the incoming positron. A combination of the e and Σ methods, the $e\Sigma$ method [19], is thus used to optimize the kinematic reconstruction in the NC measurement; Q^2 is taken from the e method and x from the Σ method. Both these variables display good resolution in the complete kinematic range and the radiative corrections remain small compared to those of the e method. The $e\Sigma$ formulae are

$$y_{e\Sigma} = \frac{2E_e}{E-p_z} y_\Sigma \qquad Q^2_{e\Sigma} = \frac{P^2_{T,e}}{1-y_e} \qquad x_{e\Sigma} = \frac{P^2_{T,e}}{s\,y_\Sigma(1-y_\Sigma)}\,. \tag{6}$$

2.2 Detector and Trigger

The H1 detector [20] is a nearly hermetic multi-purpose apparatus built to investigate ep scattering. The high Q^2 cross-section measurements reported here rely primarily on the tracking system, on the Liquid Argon (LAr) calorimeter, on the luminosity detectors, and to a lesser extent on the backward calorimeter. These components are described briefly below.

The tracking system includes the central and forward tracking chambers. These detectors are placed around the beam-pipe at z positions between -1.5 and 2.5 m. A superconducting solenoid, which surrounds both the tracking system and the LAr calorimeter, provides a uniform magnetic field of 1.15 T. The central jet chamber (CJC) consists of two concentric drift chambers covering a polar angular range from 25° to 155°. Particles crossing the CJC are measured with a transverse momentum resolution of $\delta P_T/P_T < 0.01 \cdot P_T/\mathrm{GeV}$. To improve the determination of the z coordinate of the tracks, two polygonal drift chambers with wires perpendicular to the z-axis placed at radii of 18 (CIZ) and 47 cm (COZ) are used. The forward tracking detector measures charged particles emitted in an angular range from 7° to 25°. It is used in this analysis to determine the interaction vertex for events with no track in the CJC.

The LAr calorimeter [21], which surrounds the tracking system in the central and forward regions, covers an angular region between 4° and 154°. It is divided in 8 wheels along the z-axis, which are themselves subdivided in φ in up to 8 modules, separated by small regions with inactive material ("z-cracks" and "φ-cracks" respectively). The calorimeter consists of an electromagnetic section with lead absorber plates and a hadronic section with stainless steel

absorber plates. Both sections are highly segmented in the transverse and longitudinal directions with about $44\,000$ cells in total. The electromagnetic part has a depth between 20 and 30 radiation lengths ($X_\circ$). The total depth of the calorimeter varies between 4.5 and 8 interaction lengths (λ_I). The systematic uncertainty of the electromagnetic (hadronic) energy scale of the LAr calorimeter is between 0.7 and 3% (2%) (section 2.6).

In the backward region a lead/scintillating fibre calorimeter (SPACAL) [22] was installed in 1995 to replace the previous lead/scintillator electromagnetic calorimeter (BEMC). The new calorimeter has both an electromagnetic and a hadronic section with a total depth of about $2\lambda_I$, compared with the $1\lambda_I$ depth of the BEMC. Together with the LAr calorimeter, its angular acceptance ($154^\circ < \theta < 177.8^\circ$) makes possible complete coverage for the detection of the hadronic final state in the H1 apparatus apart from the remnants of the proton. The uncertainty in the measurement of hadronic energy in the SPACAL is 7%, compared with 15% for the BEMC which was operational when the 1994 data were taken. The influence of the backward calorimeter on the analysis presented here is small.

The LAr and backward calorimeters are surrounded by the Instrumented Iron [20] which is used for muon identification and for the measurement of hadronic energy leaking from the other calorimeters. In this analysis it is used to reject muon induced background.

The ep luminosity is determined by comparison of the QED cross-section for the bremsstrahlung reaction $ep \rightarrow ep\gamma$ with the measured event rate. The photon is detected in a calorimeter (photon "tagger") close to the beam-pipe which is situated at a large distance from the main detector ($z = -103$ m). The precision of the luminosity determination is 1.5% [23].

An electron tagger is placed at $z = -33$ m adjacent to the beam-pipe. It is used to check the luminosity measurement and to provide information on $ep \rightarrow eX$ events at very low Q^2 (photoproduction) where the positron scatters through a small angle ($\pi - \theta_e < 5$ mrad).

The "trigger" for the high Q^2 events uses mainly information from the LAr calorimeter. In NC events the positron initiates a trigger "tower" [20, 21] of electromagnetic energy which points towards the event vertex. Above the threshold energy of the analysis (11 GeV) the trigger efficiency is $\geq 99.5\%$. For CC events the missing transverse momentum $P_T^{\rm miss}$, determined from the vector sum of the calorimeter towers[3], is used as the trigger. During 1997 data taking, a trigger which used track information supplemented the $P_T^{\rm miss}$ trigger in events with small missing transverse momentum and large angles of the hadrons. The combined efficiency of these triggers [24] for the CC analysis reaches 98% for a missing transverse momentum $P_T^{\rm miss}$ above 25 GeV, and is about 50% at the minimum $P_T^{\rm miss}$ of the analysis (12 GeV).

2.3 Event Simulation

In order to determine acceptance corrections and background contributions for the DIS cross-section measurements, the detector response to events produced by various Monte Carlo generation programs is simulated in detail using a program based on GEANT [25]. These simulated events are then subject to the same reconstruction and analysis chain as the real data.

[3]For CC events this scalar quantity $P_T^{\rm miss}$ is equal to $P_{T,h}$.

DIS processes are generated using the DJANGO [26] program which is based on HERACLES [27] for the electroweak interaction and on LEPTO [28], using the colour dipole model as implemented in ARIADNE [29] to generate the QCD dynamics. The JETSET [30] program is used for the hadron fragmentation. The implementation of HERACLES in DJANGO includes the real bremsstrahlung from the positron and the effects of vacuum polarization [31]. The simulated events are produced with the MRSH [32] parton distributions, reweighted to the H1 NLO QCD Fit described in section 3.2 which then gives a better description of the data.

The NC (CC) analysis makes use of a sample of simulated events corresponding to an integrated luminosity of about 3 (75) times that of the data. At $Q^2 > 1000\ \mathrm{GeV}^2$ and $x > 0.3$ additional samples of simulated events are included, which amount to between 10 and 1000 times the integrated luminosity of the data.

The main background contribution to NC and CC processes is due to photoproduction (γp) events. These are simulated using the PYTHIA [33] generator with GRV leading order parton distribution functions for the proton and photon [34]. This background is described in detail in section 2.5.2.

Further potential background contributions resulting from the following ep processes have been simulated: 1) elastic and inelastic QED Compton events can fake NC processes and are generated by the COMPTON [35] program; 2) elastic and inelastic $\gamma\gamma$ processes producing pairs of leptons (l), $ep \rightarrow ep\ l^+\ l^-(eX\ l^+\ l^-)$, are generated using the LPAIR [36] program (processes with $l^\pm = e^\pm$ can contribute to the NC sample, while processes with $l^\pm = \mu^\pm$ are more likely to contribute in the CC sample); 3) prompt photon production with $\gamma - e$ misidentification can fake NC events and is generated as a dedicated PYTHIA sample; 4) real production of heavy gauge bosons, $ep \rightarrow eXW^\pm(eXZ)$, followed by leptonic decays of the W or Z is generated using the EPVEC [37] program. These processes were found to produce only a small ($\lesssim$1%) contamination in the measured (x, Q^2) domain. They have been taken into account and will not be discussed henceforth.

2.4 Event Selection

For CC events the selection is based on the observation of large P_T^{miss}, which is assumed to be the transverse momentum p_T^ν carried by the outgoing neutrino. For NC events it is based on the identification of a scattered positron with large $P_{T,e}$. For both CC and NC events an event vertex, which is reconstructed using central or forward tracks, is required to be within $\pm 35\ \mathrm{cm}$ of its nominal position. Fiducial (NC) and kinematic cuts (CC and NC) are then applied. The reconstruction of the kinematic variables for each selection follows the methods described in section 2.1, and uses the measurements of the positron and the hadronic final state which are described in section 2.6.

CC events are selected as follows:

- the P_T^{miss} is required to be greater than $12\ \mathrm{GeV}$;
- the inelasticity y_h is required to be in the range 0.03 to 0.85 to restrict the measurement to a region where the kinematic reconstruction is precise;

- the ratio V_{ap}/V_p is required to be less than 0.15 to reject photoproduction background; V_p and V_{ap} are respectively the transverse energy flow parallel and antiparallel to $\vec{P}_{T,h}$; they are determined from the transverse momentum vectors $\vec{P}_{T,i}$ of all the particles i which belong to the hadronic final state according to

$$V_p = \sum_i \frac{\vec{P}_{T,h} \cdot \vec{P}_{T,i}}{P_{T,h}} \qquad \text{for} \qquad \vec{P}_{T,h} \cdot \vec{P}_{T,i} > 0 \tag{7}$$

$$V_{ap} = -\sum_i \frac{\vec{P}_{T,h} \cdot \vec{P}_{T,i}}{P_{T,h}} \qquad \text{for} \qquad \vec{P}_{T,h} \cdot \vec{P}_{T,i} < 0\,. \tag{8}$$

To identify the positron in NC events, the presence of a compact and isolated electromagnetic cluster of energy in the LAr calorimeter is required [38]. For $\theta_e > 35^\circ$ the positron candidate is validated only if it is associated with a track having a distance of closest approach to the cluster of less than 12 cm (section 2.6.1). Fiducial cuts are applied to ensure the quality of the positron reconstruction (section 2.6.2). Events are also not included if $\theta_e \gtrsim 153^\circ$, because then the electromagnetic shower of the scattered positron is not fully contained in the LAr calorimeter. The measurements are thus restricted to $Q^2 \geq 150$ GeV^2. NC events with such an identified positron are required to satisfy the following cuts:

- a cluster energy E'_e greater than 11 GeV;
- an inelasticity y_e lower than 0.9;
- a longitudinal momentum balance verifying $E-p_z$ (eq. 5) greater than 35 GeV.

These requirements minimize the size of radiative corrections applied in the analysis (section 3.1) and reduce the background due to photoproduction.

After all the different steps of the event selection, and after the additional requirements described below to reject events from background processes, the DIS data sample comprises about $75\,000$ NC events and 700 CC events.

2.5 Background Rejection

The CC and NC event samples which result from the selection procedures described in the previous section contain both non-ep background, arising from particles produced in proton-nucleus interactions and from cosmic rays, and ep-induced background.

2.5.1 Non-ep Background

Events resulting from processes other than ep collisions originate from cosmic rays, from "beam-halo muons" of the proton beam which interact in the detector material and cause electromagnetic showers, and from protons interacting with residual particles in the beam-pipe (beam-gas events) or with the beam-pipe itself (beam-wall events).

A large fraction of these background events are removed by requiring that the event time T_0, determined from the drift times of hits from tracks in the CJC, is coincident with the collision time at the ep interaction region. In the CC analysis the background is further reduced by using in addition the T_0 determined from the rise times of signals in the LAr calorimeter.

The remaining background is found to be negligible in the NC sample. Further reductions are necessary in the CC analysis in which the background mainly originates from random coincidences between soft photoproduction events and cosmic rays or beam-halo muons. The majority of these events are rejected by means of topological requirements following reconstruction of a cosmic ray or a beam-halo muon using information from the LAr and SPACAL calorimeters, the CJC and the Instrumented Iron [11, 24, 39, 40].

The inefficiency in the CC selection introduced by these requirements is determined in two different ways. A visual scan of rejected events yields an overall inefficiency for the CC selection of $5 \pm 2\%$. This result is consistent with the inefficiency obtained when using NC events in which the presence of the scattered positron is ignored. The residual contamination of non-ep induced background events in the CC sample is determined to be 3.7% by visual scanning. These events are then rejected so that the remaining uncertainty in the CC sample from non-ep background is below 0.5%.

2.5.2 ep-induced Background

The main ep-induced background in the CC sample originates from γp events and from NC events in which the scattered positron is not identified. Mismeasurement of energies and limited geometrical acceptance can in both cases lead to events which are not balanced in transverse momentum.

In CC events the energy flow is concentrated in the hemisphere opposite to the transverse momentum of the scattered neutrino, resulting in a low value for V_{ap}/V_p (eqs. 7, 8) while in γp and NC background events it is more isotropic, giving values of V_{ap}/V_p close to 0.5. This is seen in fig. 1a where the V_{ap}/V_p distribution is shown for γp events for which the scattered positron is measured in the electron tagger and which pass the CC selection, apart from the cut on V_{ap}/V_p. The observed distribution is well described in shape and normalization by the γp simulation. An error of $\pm 30\%$ on the simulation of the photoproduction background is shown on the figure.

The same distribution, shown in fig. 1b for all events which pass the CC selection apart from the cut on V_{ap}/V_p, is well described by the simulation of CC and background ($\mathrm{bg} \equiv \gamma p$ + NC) events. The cut of $V_{ap}/V_p < 0.15$, applied in the CC selection, rejects a large fraction of this

background. According to the simulation, about 70 (95)% of the CC events with $12 < P_T^{\rm miss} < 15$ GeV ($P_T^{\rm miss} > 25$ GeV) survive this cut. To evaluate the systematic uncertainty in the CC selection efficiency which is introduced by this requirement, the cut value of V_{ap}/V_p is varied between 0.13 and 0.17 in the simulation while keeping the value fixed for the data. A variation in the efficiency with which CC events are retained of 5 (2)% at low (high) $P_T^{\rm miss}$, averaged over y_h, is then observed.

In the CC analysis residual background due to NC interactions is rejected by removing events with only one track with azimuthal angle opposite to the hadronic final state ($|\varphi_{track} - \varphi_h| > 160°$). The azimuthal angle φ_h of the hadronic final state is defined by $\tan\varphi_h = p_{y,h}/p_{x,h}$. Events with large $P_T^{\rm miss}$ and isolated high momentum leptons observed recently [41] are removed in this analysis by applying the selection procedure for such events which is used there. The additional inefficiency introduced into the CC selection due to these requirements is less than 1%. The remaining contamination due to ep-induced background is evaluated from the simulation and statistically subtracted from the data. The background corresponds to about 10% at the lowest Q^2 values and less than 2% for $Q^2 > 1000$ GeV^2.

In the NC analysis after all selection cuts, the only significant background is due to events from photoproduction processes, in which the scattered positron escapes the detector along the beam-pipe and one of the particles of the hadronic final state is misidentified as the scattered positron. As in the CC case this background, determined from the simulation, is controlled using the sub-sample of about 10% of the γp events in which the scattered positron is detected

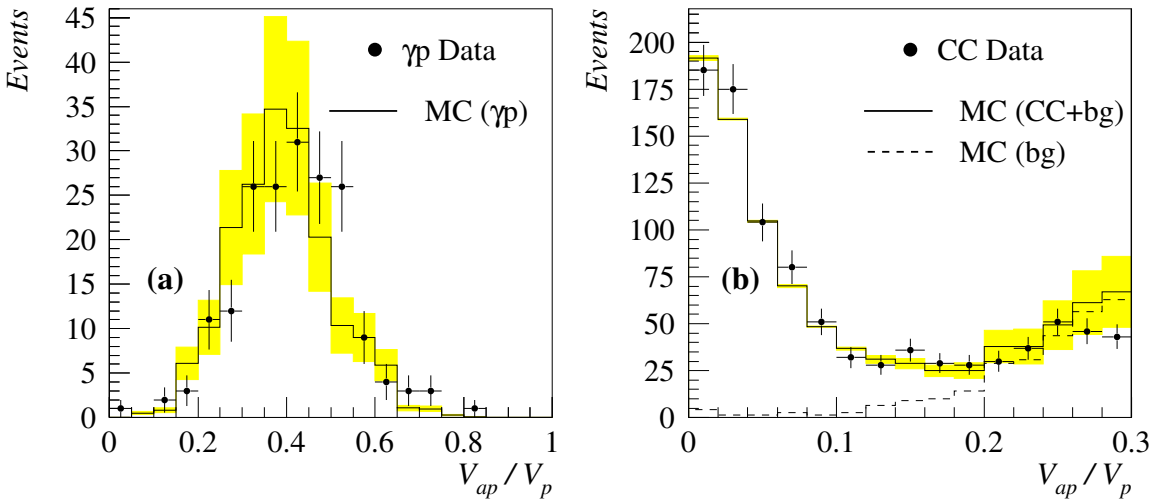

Figure 1: *(a) Distribution of V_{ap}/V_p for tagged γp events passing the CC selection except for the V_{ap}/V_p cut. The data (points) are compared to the Monte Carlo (MC) simulation (histogram) of the γp background. (b) Distribution of V_{ap}/V_p for the CC event sample. The data (points) are compared to the simulation (histogram) which includes the CC and the background* (bg $\equiv \gamma p$ + *NC) events. A cut $V_{ap}/V_p < 0.15$ is applied in the CC selection. The simulation is normalized to the integrated ep luminosity. The shaded error bands represent the systematic uncertainty of the background simulation.*

in the electron tagger, and is subtracted from the data. It amounts to less than 1% in the total sample and to at most 5% in the highest y bins at $Q^2 < 1000\ \mathrm{GeV}^2$.

2.6 Detector Alignment and Calibration

At high Q^2 the scattered positron and the hadronic final state are predominantly measured with the LAr calorimeter. From test beam data the initial electromagnetic and hadronic energy scales were established with an uncertainty of about 3% for electrons and pions of energy between 4 and $205\ \mathrm{GeV}$ [42, 43]. These energy scales were verified *in situ* at HERA using the 1994 data [6]. The tracking detectors are used wherever possible to improve these measurements by making use of their good angular precision for the scattered positron, and by making use of their good precision in both angle and momentum measurement for the determination of the hadronic final state energy. This section is concerned with the method used to reconstruct the positron angle, the absolute calibration of the positron energy, and the relative hadronic energy scale between data and simulation. More details of the energy calibration procedures can be found in [44].

2.6.1 Positron Angle Measurement

The polar angle of the scattered positron is determined using the central tracking detectors when its track is reconstructed using hits in the 3 central chambers CJC, CIZ and COZ. When the positron's track is less well constrained, the angle is determined from the position of the positron energy cluster in the LAr calorimeter and the vertex reconstructed using tracks from charged particles in the event.

By minimizing the spatial discrepancy between the positron track and the location of the calorimeter cluster, the alignment of the tracking detectors relative to the LAr calorimeter was established to within $1\ \mathrm{mm}$ in the x, y and z directions.

Following this alignment the precision of the angle measurement with the tracking detectors (with the calorimeter cluster and event vertex) is better than 1 (3) mrad. The proportion of scattered positrons in which θ_e is determined from the cluster and event vertex is about 40% in the central region. This proportion increases at smaller θ_e and is 100% for $\theta_e < 35°$. The vertex is determined from the tracking detectors with a precision of approximately $3\ \mathrm{mm}$ in z and $1\ \mathrm{mm}$ in x and y. Because the mean of the distribution of event vertices depends on the characteristics of the stored positron and proton beams, the vertex distribution is determined from the data for every beam storage, and in event simulation the vertex distribution is adjusted to follow these changes.

The θ_e distributions for the data and for the simulation are shown in fig. 2. The simulation describes the data well throughout the complete angular range.

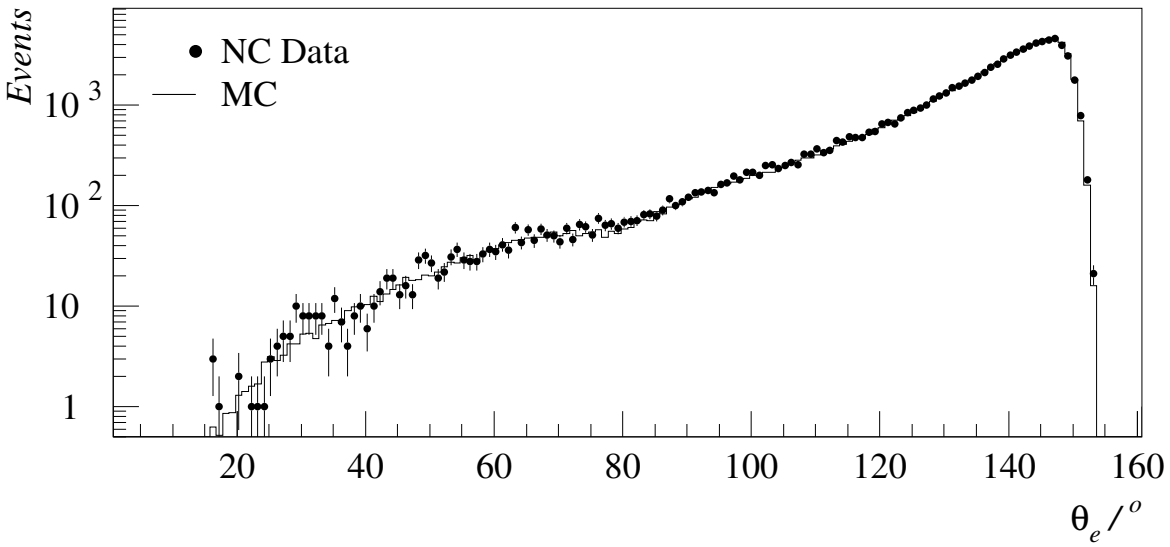

Figure 2: *Distribution of polar angle of the scattered positron. The data (points) are compared to the simulation (histogram) which is normalized to the integrated ep luminosity.*

2.6.2 Positron Energy Measurement

For the present cross-section analysis the calibration constants and their uncertainties have been improved compared to the previous H1 measurements by making use of the increased NC event sample and exploiting the overconstrained kinematic reconstruction.

Before the *in situ* calibration discussed below, the measured positron energy is corrected for energy loss in the material in front of the calorimeter (between 0.7 and $2.5 X_\circ$). Further energy loss can occur in the crack regions between the calorimeter modules in the z and φ directions. To limit the size of the corrections which occur because of the crack regions, the impact position of the positron track on the calorimeter is required to lie outside a fiducial area of $\pm 2^\circ$ around a φ-crack and ± 5 cm around the z-crack located between the CB2 and CB3 wheels of the LAr calorimeter (see fig. 3 for the angular coordinates of the seven electromagnetic wheels of the LAr calorimeter) [21].

For the *in situ* calibration of the barrel region ($\theta_e > 40^\circ$), only the NC events with $y_\Sigma < 0.3$ ($y_\Sigma < 0.5$) in the region of $80^\circ \lesssim \theta_e \lesssim 153^\circ$ ($40^\circ \lesssim \theta_e \lesssim 80^\circ$) are used. For these y values the energy of the scattered positron is predicted precisely by the double-angle (DA) method [45] in which the kinematic variables are determined solely from θ_e and γ_h. The calibration is achieved by constraining the mean of the $E'_e/E_{\rm DA}$ distribution to 1 via small local adjustments of the calibration constants. These constants are determined in finely segmented z and φ regions defined by the impact position of the positron track on the LAr calorimeter. An analogous procedure was performed for the simulation. The calibration constants vary typically by $\pm 1\%$ around their average values, except in the regions close to the z-cracks, where the corrections may reach up to 8% [24]. Outside these regions the calibrated energy response is described by the simulation within 0.5%. The absolute calibration is obtained by applying in addition corrections of about 1%, derived from the simulation, which take into account effects from initial state QED radiation and small biases originating from the imperfect γ_h reconstruction.

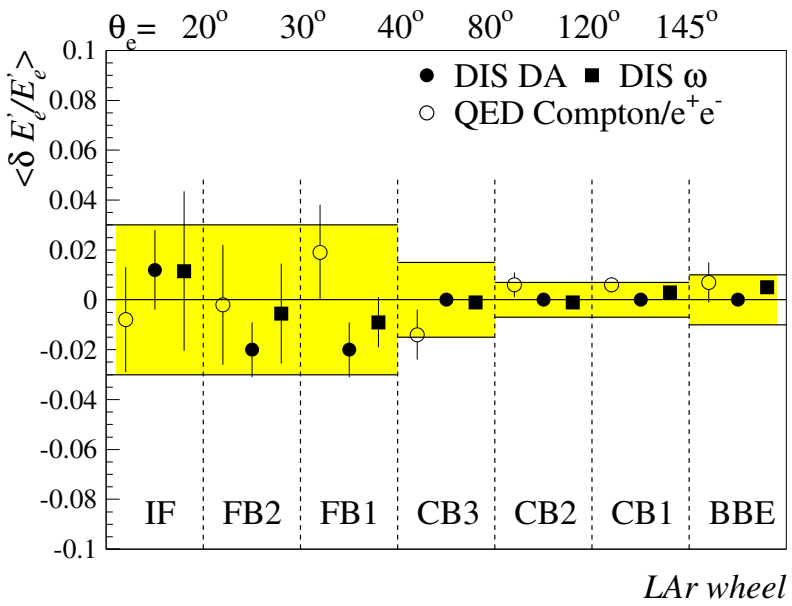

Figure 3: *Comparison of the electromagnetic energy scale as determined by different calibration methods. Shown is* $\langle \delta E'_e / E'_e \rangle$*, the mean fractional energy shift of the different methods from the absolute energy scale. The shaded error band shows the systematic uncertainty on the energy scale quoted on this measurement, which varies from* 0.7 *to* 3%*, depending on the position in the detector.*

Due to the limited number of events with positrons in the forward region ($\theta_e < 40°$) two event samples, elastic QED Compton and exclusive two photon e^+e^- pair production, are used in addition to the DIS events. The requirement of transverse momentum balance allows the energy of the more forward electromagnetic energy deposit to be determined from the well calibrated backward cluster. For the DIS events the ω kinematic reconstruction method [46] is used to determine the calibration constants instead of the DA method since it is by design less sensitive to the effects of initial state QED radiation and is therefore more reliable when there are low statistics. A single calibration constant is determined for the entire forward region.

After the application of these calibration procedures, the positron energy scale is checked for each calorimeter wheel using the elastic QED-Compton and e^+e^- event sample and, separately, the ω method for the DIS sample. The results from all the different methods are found to be in good agreement, as shown in fig. 3. An error of ± 0.7 $(1.0, 1.5, 3.0)\%$ on the absolute electromagnetic energy scale of the CB1–CB2 (BBE, CB3, FB1–IF) wheels of the detector is therefore assigned. The uncertainties in the electromagnetic energy scale increase towards the forward region due to the decreasing number of events. The resulting energy spectra are presented for $Q^2 > 150$ (5000) GeV^2 in fig. 4a(b), and are well described by the simulation within the normalization uncertainty of $\pm 1.5\%$.

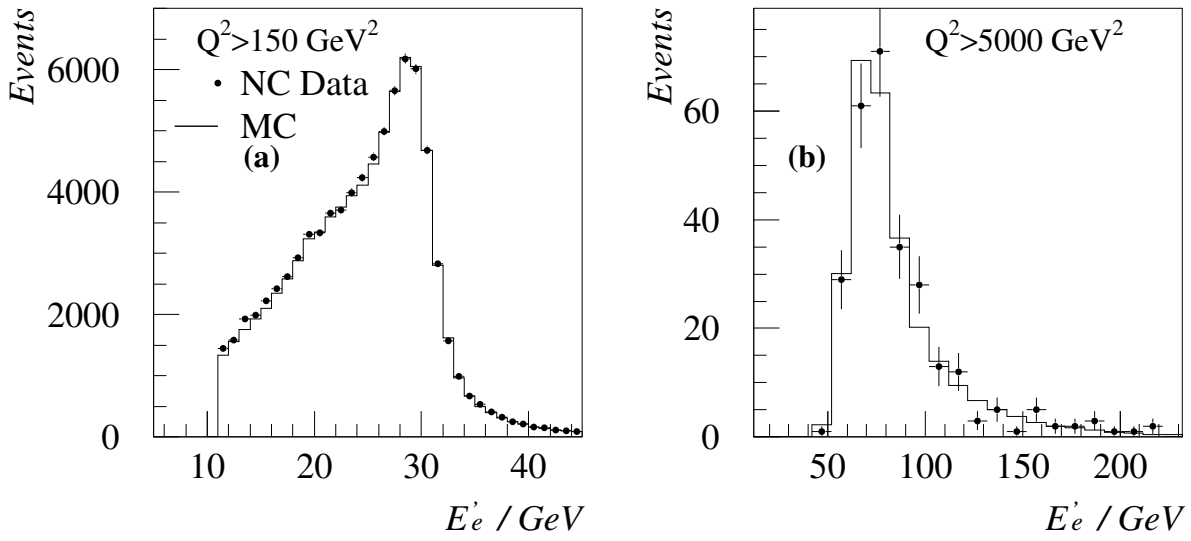

Figure 4: *Energy spectrum of the scattered positron at (a)* $Q^2 > 150\ \mathrm{GeV}^2$*, and (b)* $Q^2 > 5000\ \mathrm{GeV}^2$*. The data (points) are compared to the simulation (histogram) which is normalized to the integrated* ep *luminosity.*

2.6.3 Hadronic Energy Measurement

The optimal measurement of the hadronic final state energy is obtained after applying specific techniques to the reconstruction of the calorimeter and tracking information, as described in the following.

Since the H1 LAr calorimeter is non-compensating, weighting algorithms are applied to the hadronic clusters in order to improve the energy resolution [43, 47]. A further improvement in energy resolution of about 10 to 20%, for events having a $P_{T,h}$ between 10 to 25 GeV, is obtained by using a combination of the energies of low transverse momentum particles ($P_T < 2\ \mathrm{GeV}$) measured in the central tracking detector with the energies deposited by other particles of the hadronic final state measured in the calorimeter. To avoid "double counting", the energy measured in the electromagnetic (hadronic) LAr calorimeter in a cylinder of $15\ (25)\mathrm{cm}$ in radius around the axis given by the direction of a low transverse momentum track is not included, except if the total energy in the cylinders is greater than the energy of the track, in which case only the calorimetric measurement is used. The fraction of y_h measured by each of the subdetectors (LAr, tracks, SPACAL) is shown in fig. 5a to be well described by the simulation in the range $0.005 \leq y_h \leq 0.9$. The contribution of the SPACAL calorimeter is below 10% except at high y.

At low $y \lesssim 0.05$, where hadrons are produced in the forward direction and little energy is deposited in the calorimeter, the measurement of the kinematic variables is distorted by the presence of "noise" in the calorimeter cells due either to the electronics of the calorimeter readout, or to the secondary scattering of final state particles into the calorimeter. Both sources of noise are included in the simulation. The noise is reduced by suppressing isolated low energy deposits [48], which results in a significant improvement of the reconstruction of the kinematic

variables at low y. The fraction of y_h identified as noise is shown in fig. 5a to be described by the simulation. The effect of a variation of $\pm 25\%$ of the subtracted noise contribution is included in the systematic error.

The *in situ* calibration of the hadronic energy scale [44] is made by comparing the transverse momentum of the precisely calibrated positron (section 2.6.2) to that of the hadronic system in NC events. Calibration constants are determined for each of the 7 electromagnetic and 8 hadronic wheels. The calibration factor for each wheel is evaluated using the ratio $P_{T,h}/P_{T,e}$ of each event weighted with the fraction of $P_{T,h}$ carried by the wheel. The calibration constants are adjusted iteratively until the average ratio $\langle P_{T,h}/P_{T,e} \rangle$ for the data equals that of the simulation

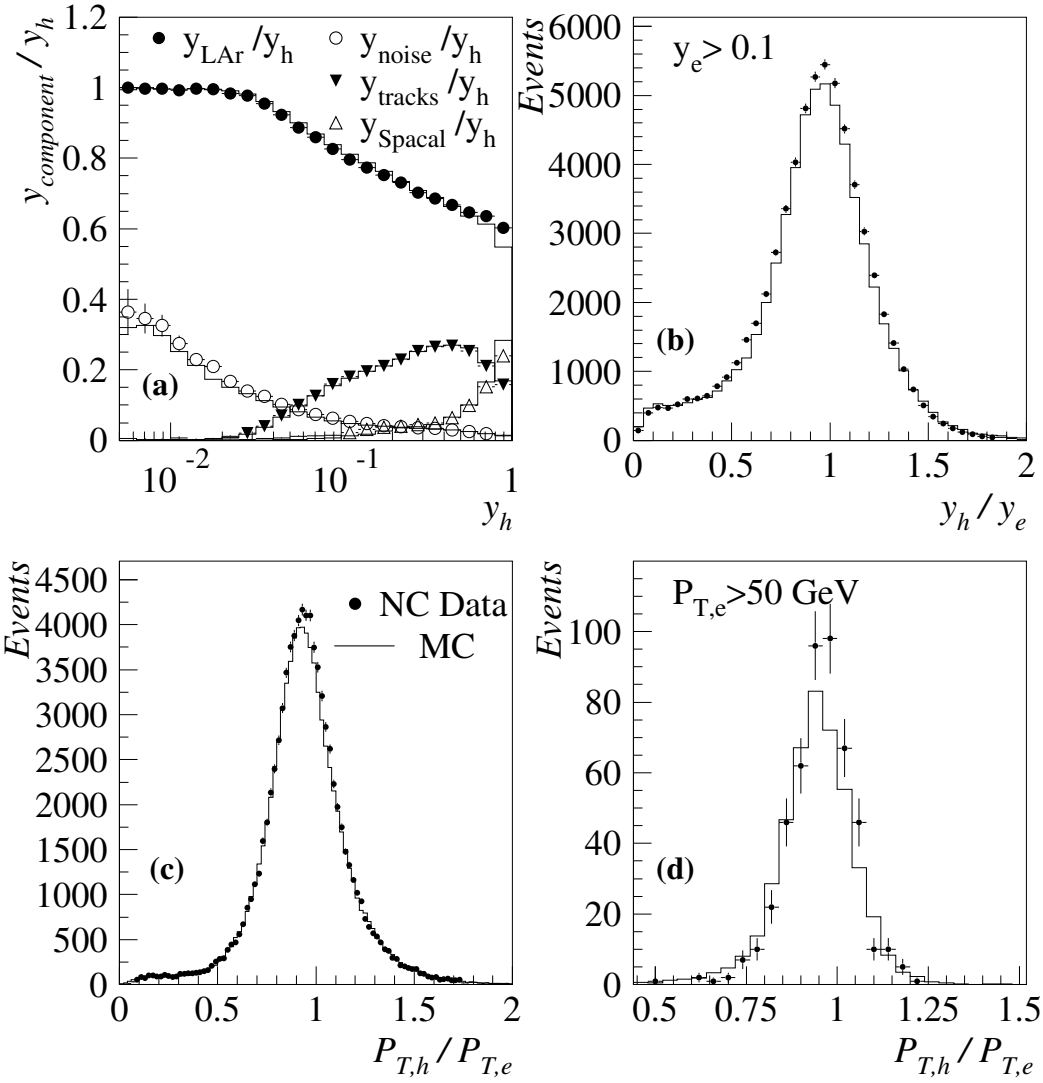

Figure 5: *(a) Distribution of the fraction of y_h contributed by the tracks (y_{tracks}), the LAr (y_{LAr}) and the SPACAL calorimeters (y_{Spacal}), and the fractional contribution of the subtracted noise (y_{noise}). (b) Distribution of y_h/y_e for $y_e > 0.1$. (c) Distribution of $P_{T,h}/P_{T,e}$ for the complete NC sample, (d) for the sub-sample at $P_{T,e} > 50$ GeV. The data (points) are compared to the simulation (histogram) which is normalized to the integrated ep luminosity.*

in all regions of the detector.

Detailed studies of the dependence of $P_{T,h}/P_{T,e}$ and y_h/y_e on P_T and γ_h justify a systematic uncertainty on the relative hadronic energy scale of the LAr calorimeter of 2%. A further confirmation of this scale uncertainty is obtained using the topology of the NC events which can be divided in two samples. In the sample of events with only one well reconstructed jet, the jet direction directly determines the wheel containing the maximum amount of transverse energy, allowing the corresponding wheel calibration constant to be checked precisely. In the sample of events with a multijet topology the $P_{T,h}/P_{T,e}$ distribution has also been observed to be better described by the simulation after applying the hadronic calibration.

The dependence of the calibration on the usage of two different hadronic final state models in the simulation, one which assumes QCD matrix elements and parton showers (MEPS) as implemented in LEPTO and the other which assumes the colour dipole model in its ARIADNE implementation, has been studied and found to be negligible.

The quality of the resulting hadronic final state reconstruction is illustrated in fig. 5b,c,d. In fig. 5b the y_h/y_e distribution for $y_e > 0.1$ is shown. In this distribution the hadronic energy enters with a different angular weight than in the $P_{T,h}/P_{T,e}$ distribution. The agreement observed between data and simulation shows that the hadronic calibration is valid for the energy itself, and not only for the transverse energy. Fig. 5c(d) shows the $P_{T,h}/P_{T,e}$ distribution in the complete NC event sample (with $P_{T,e} > 50$ GeV). In both distributions, the data are described by the simulation within the quoted 2% uncertainty.

3 Cross-Section Measurement Procedure

3.1 Cross-Sections and Structure Functions

In this section the cross-section definitions are introduced together with the procedure adopted for the treatment of radiative corrections. The measured cross-sections are:

- the NC (CC) double differential cross-section $d^2\sigma_{NC(CC)}/dxdQ^2$;
- the NC (CC) single differential cross-sections $d\sigma_{NC(CC)}/dQ^2$ and $d\sigma_{NC(CC)}/dx$.

These cross-sections are presented in this paper after corrections for the effects of QED radiation have been made. They are derived from the "initial" cross-sections which are determined using the measurement procedure described in section 3.3. Thus the double differential NC (CC) cross-sections are defined as

$$\frac{d^2\sigma_{NC(CC)}}{dx\ dQ^2} = \left(\frac{d^2\sigma_{NC(CC)}}{dx\ dQ^2}\right)_{initial} \left[1 + \delta^{qed}_{NC(CC)}(x, Q^2)\right]^{-1} . \tag{9}$$

The δ^{qed}_{NC} term includes the effects of photon emission from the lepton line, the effects of the photonic lepton vertex corrections combined with the self energies of the external fermion lines,

and the effects of the fermion loops of the exchanged photon self energy. The δ^{qed}_{CC} term includes the leptonic part of the $\mathcal{O}(\alpha)$ photonic correction to CC processes [49, 50]. These radiative corrections[4] are calculated using DJANGO and verified with the HECTOR [51] program. The weak radiative corrections $\delta^{weak}_{NC(CC)}$, which are defined in [52] and which are small (of the order of 1%), have not been applied to the measured cross-sections.

When extracting the structure functions of the proton from cross-section measurements, the weak radiative corrections are, however, applied. The Born cross-section is then defined as

$$\left(\frac{d^2\sigma_{NC(CC)}}{dx\ dQ^2}\right)_{Born} = \frac{d^2\sigma_{NC(CC)}}{dx\ dQ^2} \quad \left[1+\delta^{weak}_{NC(CC)}(x,Q^2)\right]^{-1} . \tag{10}$$

The Born double differential NC cross-section for $e^+p \to e^+X$ can be written as

$$\left(\frac{d^2\sigma_{NC}}{dx\ dQ^2}\right)_{Born} = \frac{2\pi\alpha^2}{x}\left(\frac{1}{Q^2}\right)^2 \ \phi_{NC}(x,Q^2)\,, \tag{11}$$

where

$$\phi_{NC}(x,Q^2) = Y_+\tilde{F}_2(x,Q^2) - Y_- x\tilde{F}_3(x,Q^2) - y^2\tilde{F}_{_L}(x,Q^2). \tag{12}$$

Here α is the fine structure constant taken to be $\alpha \equiv \alpha(Q^2=0)$. The "structure function term" $\phi_{NC}(x,Q^2)$ is a linear combination of the $\tilde{F}_2$ structure function, the longitudinal structure function $\tilde{F}_{_L}$, and the $x\tilde{F}_3$ structure function which in the Standard Model is significant only when Q^2 is sufficiently large to render Z° exchange non-negligible. The helicity dependences of the electroweak interactions are contained in the functions $Y_\pm = 1 \pm (1-y)^2$.

In leading order QCD, the structure function term is simply related to the sum of the light quark densities, weighted with the squared quark charges, when neglecting Z° exchange:

$$(\phi_{NC})_{LO} = \left[1+(1-y)^2\right]\ x\ \left[\frac{4}{9}\left(u+c+\bar{u}+\bar{c}\right)+\frac{1}{9}\left(d+s+\bar{d}+\bar{s}\right)\right] . \tag{13}$$

At high x the structure function term ϕ_{NC} depends predominantly on the valence distribution of the u quark.

For unpolarized beams, the structure functions $\tilde{F}_2$ and $x\tilde{F}_3$ can be decomposed, taking into account Z° exchange, as [53]

$$\tilde{F}_2 \equiv F_2 - v\,\frac{\kappa_w Q^2}{(Q^2+M_Z^2)}\ F_2^{\gamma Z} + (v^2+a^2)\left(\frac{\kappa_w Q^2}{Q^2+M_Z^2}\right)^2 F_2^Z \tag{14}$$

$$x\tilde{F}_3 \equiv - a\,\frac{\kappa_w Q^2}{(Q^2+M_Z^2)} xF_3^{\gamma Z} + (2va)\left(\frac{\kappa_w Q^2}{Q^2+M_Z^2}\right)^2 xF_3^Z\,, \tag{15}$$

where M_Z is the mass of the Z°, $\kappa_w = 1/(4\sin^2\theta_w\cos^2\theta_w)$ is a function of the Weinberg angle (θ_w), and v and a are the vector and axial vector couplings of the electron to the Z°.

[4]The radiative corrections due to the exchange of two or more photons between the lepton and the quark lines are small and are included in the systematic uncertainty of the radiative corrections.

They are related to the weak isospin of the electron, $I_3 = -\frac{1}{2}$, namely $v = I_3 + 2\sin^2\theta_w$ and $a = I_3$ [54]. The electromagnetic structure function F_2 originates from photon exchange only, and the functions F_2^Z (xF_3^Z) and $F_2^{\gamma Z}$ ($xF_3^{\gamma Z}$) are the contributions to $\tilde{F}_2$ ($x\tilde{F}_3$) due to Z° exchange and γZ° interference respectively. Note that for unpolarized beams, $\tilde{F}_2$ is the same for electron and for positron scattering, while the $x\tilde{F}_3$ term in eq. 12 changes sign.

The NC "reduced cross-section" is defined from the measured $d^2\sigma_{NC}/dxdQ^2$ in order to reduce the strong Q^2 dependence originating from the propagator:

$$\tilde{\sigma}_{NC}(x,Q^2) \equiv \frac{1}{Y_+}\,\frac{Q^4\,x}{2\pi\alpha^2}\,\frac{d^2\sigma_{NC}}{dxdQ^2}\,. \tag{16}$$

In the major part of the (x,Q^2) domain F_2 is the dominant component of the structure function term $\phi_{NC}(x,Q^2)$, and $\tilde{\sigma}_{NC}$ is conveniently expressed as

$$\tilde{\sigma}_{NC} \;=\; F_2\,(1+\Delta_{F_2}+\Delta_{F_3}+\Delta_{F_L})\,(1+\delta_{NC}^{weak}) \;=\; F_2\,(1+\Delta_{all})\,, \tag{17}$$

where the Δ_{F_2} and Δ_{F_3} terms originate from the $F_2^{\gamma Z}$, F_2^Z and $F_3^{\gamma Z}$, F_3^Z functions defined in eq. 14 and 15, and the Δ_{F_L} term from the longitudinal structure function $\tilde{F}_{_L}$. Values of each of these terms obtained from the NLO QCD Fit described in section 3.2 are given in table 4.

In the kinematic range investigated the effects of Z° exchange ($\Delta_{F_2}+\Delta_{F_3}$) on $\tilde{\sigma}_{NC}$ are expected to be $\leq$ 5% for $Q^2 < 5000$ GeV^2 (table 4). It is thus possible to extract F_2 from the measured cross-section with little uncertainty in this Q^2 range. At higher Q^2 values the contribution of the $x\tilde{F}_3$ term results in a significant reduction of the e^+p cross-section. The determination of F_2 then relies strongly on the calculation of Δ_{F_2} and Δ_{F_3}. In QCD calculations the Δ_{F_L} term is small and decreases at constant y with increasing Q^2. It reaches 6% for $y \geq 0.65$ and $Q^2 \leq 1500$ GeV^2 but is negligible for $y \lesssim 0.4$.

The Born double differential CC cross-section for $e^+p \to \bar{\nu}X$ can be written as

$$\left(\frac{d^2\sigma_{CC}}{dx\;dQ^2}\right)_{Born} = \frac{G_F^2}{2\pi x}\left(\frac{M_W^2}{M_W^2+Q^2}\right)^2\phi_{CC}(x,Q^2)\,, \tag{18}$$

where G_F is the Fermi coupling constant and the structure function term $\phi_{CC}(x,Q^2)$ can be decomposed into structure functions in a similar way as $\phi_{NC}(x,Q^2)$ [55].

For CC interactions a reduced cross-section is also introduced:

$$\tilde{\sigma}_{CC}(x,Q^2) \equiv \frac{2\pi x}{G_F^2}\left(\frac{M_W^2+Q^2}{M_W^2}\right)^2\frac{d^2\sigma_{CC}}{dxdQ^2}\,. \tag{19}$$

It is directly related to the CC structure function term by

$$\phi_{CC}(x,Q^2)\left[1+\delta_{CC}^{weak}(x,Q^2)\right] = \tilde{\sigma}_{CC}(x,Q^2)\,. \tag{20}$$

In leading order QCD, neglecting the effect of quark mixing and the contribution of heavier quarks, the CC structure function term for e^+p scattering is related to the quark densities:

$$(\phi_{CC})_{LO} = x\;\left[(\bar{u}+\bar{c})+(1-y)^2(d+s)\right]\,. \tag{21}$$

At high x the structure function term ϕ_{CC} depends predominantly on the valence distribution of the d quark.

3.2 QCD Analysis Procedure

Comparison of the Standard Model with the measurements of the NC and CC ep cross-sections depends both on the model's explicit predictions for the interaction of a positron with a quark and on the partonic content of the proton. The parameters of the electroweak theory which describes positron-quark scattering in the Standard Model have been measured precisely, and are therefore fixed to their world average values [54] in this comparison. The parton distribution functions (PDFs), which describe the partonic structure of the proton, are not predicted by QCD and so must be obtained from the data. In order to obtain the PDFs together with their uncertainties, two NLO QCD fits are performed:

- the first fit (Low Q^2 Fit) is made with published low Q^2 DIS data; the proton (F_2) and deuteron (F_2^d) data from the BCDMS [4] and NMC [5] experiments are used, together with the 1994 F_2 measurements of H1 [6] at $Q^2 < 150\ \mathrm{GeV}^2$;
- the second fit (NLO QCD Fit) includes the high Q^2 NC and CC double differential cross-sections presented in this paper in addition to the datasets used in the Low Q^2 Fit.

Since the emphasis of this study is on the new data entering the fit which are at high Q^2, far above the squared masses of the charm (c) and bottom (b) quark, an approach is used in which all quarks are taken to be massless within the DGLAP equations and a cut of $Q^2 > 10\ \mathrm{GeV}^2$ is applied to the datasets. At high x and low W^2 ($W^2 \equiv Q^2[1-x]/x$) non-perturbative effects may have a large influence. Therefore only the data having $W^2 \geq 20\ \mathrm{GeV}^2$ and $x < 0.7$ are used in the fits. The fixed target data are corrected for target mass effects using the Georgi-Politzer approach [56], and for deuteron binding effects using the parameterization obtained with the method of [57] applied to SLAC measurements [58]. The effect of the deuteron corrections on the fit result are negligible for NC and up to 7% (at $x = 0.4$) for CC.

For these fits, the DGLAP evolution equations [10] are solved in the NLO $\overline{MS}$ factorization scheme using the QCDNUM [59] program. The results obtained have been cross-checked using an independent program [60]. The strong coupling constant α_s is evolved according to QCD with the constraint $\alpha_s(M_Z^2) = 0.118$. A starting scale of $Q_0^2 = 4\ \mathrm{GeV}^2$ is taken at which four PDFs are parameterized. These are the u and d valence quarks (xu_v and xd_v), the gluon (xg), and the sea quark densities ($xS \equiv 2x[\bar{u}+\bar{d}+\bar{s}+\bar{c}]$). An asymmetry between the $\bar{d}$ and $\bar{u}$ PDFs is enforced by using the $\bar{d}-\bar{u}$ parameterization from [61] taking into account the different starting scale. The strange (s) quark density is constrained to be $\bar{s} = \bar{u}/2$ at Q_0^2 [62]. The xc contribution is normalized to 2% of the sea quark density at Q_0^2 since this gives a good description of the H1 measurements [63] of the charm induced structure function F_2^c. The xb density is evolved according to the DGLAP equations assuming that $b(x, Q^2) = 0$ for $Q^2 < 25\ \mathrm{GeV}^2$.

The functional forms of the parton densities are parameterized as

$$xu_v(x,Q_0^2) = A_{u_v}x^{B_{u_v}}(1-x)^{C_{u_v}}(1+D_{u_v}x^{E_{u_v}}) \quad (22)$$

$$xd_v(x,Q_0^2) = A_{d_v}x^{B_{d_v}}(1-x)^{C_{d_v}}(1+D_{d_v}x^{E_{d_v}}) \quad (23)$$

$$xS(x,Q_0^2) = A_S x^{B_S}(1-x)^{C_S} \quad (24)$$

$$xg(x,Q_0^2) = A_g x^{B_g}(1-x)^{C_g}\,. \quad (25)$$

The parameters A_{u_v} and A_{d_v} are determined by enforcing the valence counting rules which require $\int_0^1 u_v dx = 2$ and $\int_0^1 d_v dx = 1$. The momentum sum rule allows the determination of one further normalization parameter, taken to be A_g.

The fits are performed using the MINUIT [64] program which minimizes the χ^2 defined from the data value ($f_{i,j}^{data}$) and the theoretical expectation ($f_{i,j}^{theo}$) of the measured point i in the dataset j, normalized by the quadratic sum ($\oplus$) of its statistical ($\delta f_{i,j}^{sta}$) and uncorrelated systematic ($\delta f_{i,j}^{unc}$) errors:

$$\chi^2 = \sum_{j=1}^{N_{dataset}} \left[\sum_{i=1}^{N_j^{data}} \left(\frac{f_{i,j}^{data} \times (1 + \delta\mathcal{L}_j/\mathcal{L}_j) - f_{i,j}^{theo}}{\delta f_{i,j}^{sta} \oplus \delta f_{i,j}^{unc}} \right)^2 + \left(\frac{\delta\mathcal{L}_j}{\delta\mathcal{L}_j^0} \right)^2 \right] . \quad (26)$$

The number of datasets and the number of data points in a dataset j are defined here as $N_{dataset}$ and N_j^{data}. The terms $\delta\mathcal{L}_j^0/\mathcal{L}_j$ are the luminosity uncertainties of each dataset j (1.5% for the high Q^2 data, 1.5% for the H1 1994 data, 3% for BCDMS, 2.5% for NMC). The terms $(1 + \delta\mathcal{L}_j/\mathcal{L}_j)$ are the normalizations of the datasets which are allowed to vary according to the quoted luminosity uncertainties

The results of the Low Q^2 Fit are presented in table 1 in which the χ^2 is given for each dataset, together with their optimal relative normalization, according to the criteria discussed above. The total χ^2 per degree of freedom (ndf) is $548/(529-13) = 1.06$ when considering the uncorrelated error of the data (obtained from the quadratic sum of the statistical and systematic errors which are uncorrelated from one bin to another) as given in eq. 26. If the χ^2/ndf is recalculated using the total error of the data (obtained by adding the bin to bin correlated systematic error in quadrature to the uncorrelated error) its value decreases to 0.78. The results of the NLO QCD Fit are presented in section 4.1.

Experiment	H1 94	BCDMS-p	BCDMS-D	NMC-p	NMC-D	Total
data points	77	139	133	90	90	529
χ^2 (unc. err.)	67	102	111	143	125	548
χ^2 (total err.)	39	89	98	93	77	396
normalization	1.01	0.97	0.98	0.99	0.99	

Table 1: *Results of the Low Q^2 Fit. For each experiment the following quantities are given: the number of data points, the contribution to the χ^2 using the uncorrelated errors of the data (unc. err.) as obtained from the statistical errors and uncorrelated systematic errors added in quadrature, the contribution to the χ^2 using the total errors and the optimal normalization according to the fit.*

The uncertainty on the Standard Model expectation which is used to interpret the data in section 4 is estimated from the experimental errors of the data points and by varying the theoretical assumptions of the QCD fit.

The "experimental error of the fit" is obtained by adding in quadrature the error from the QCD fit (performed with uncorrelated errors) to the contributions due to each bin to bin correlated systematic errors on the measurement. These correlated systematic errors are taken into

account by repeating the QCD fit after varying the data points coherently under the influence of each error source separately.

The "theoretical error of the fit" is obtained by repeating the QCD fit after varying each of the fit assumptions in turn: the value of $\alpha_s(M_z)$ is varied by ± 0.003; the $s/\bar{s}$ contribution is changed by $\pm 25\%$; the $c/\bar{c}$ contribution at the starting scale is multiplied by a factor of 2; an uncertainty of $\pm 50\%$ of the deuteron binding corrections is considered; the treatment of the $\bar{d}/\bar{u}$ asymmetry is changed to that given in [65] taking into account the different starting scale; the Q^2 cut applied to the data is raised to $15\ \mathrm{GeV}^2$. All the resulting differences, with respect to the nominal fit, are added in quadrature to form an estimate of the theoretical error of the fit.

The "total error of the fit" is obtained by summing in quadrature these experimental and theoretical errors and is taken as the uncertainty on the Standard Model expectation. This procedure is also used in the determination of the QCD uncertainty for the fit of the CC cross-section to extract the W boson mass as described in section 4.8.

3.3 Experimental Procedure for the Cross-Section Measurement

The NC and CC cross-sections are evaluated in bins of the (x, Q^2) plane from the number of events which pass the selection criteria (section 2.4), normalized to the integrated ep luminosity, and corrected for acceptance and bin to bin migrations with the simulation. The simulation is found to reproduce well the resolution of the measured kinematic variables, as well as the efficiencies of the selection cuts within the errors described in section 3.4. Whenever there is a difference, the selection efficiency in the simulation is adjusted to that of the data. These bin averaged cross-sections are then converted to cross-sections at chosen bin centres using corrections obtained from the NLO QCD Fit.

The NC data are binned in Q^2 with 10 bins per order of magnitude, except at $Q^2 \geq 3000\ \mathrm{GeV}^2$, for which a binning twice as large is adopted to account for the rapidly decreasing number of events. The data are binned in x with 5 bins per order of magnitude, except at $x > 0.13$ and $Q^2 \leq 400\ \mathrm{GeV}^2$, for which a coarser binning is chosen to accommodate the degradation of the x resolution at very low y (< 0.02). The CC data are binned with 3 bins per order of magnitude in both Q^2 and x. The coarser CC binning is due to the smaller statistics of the CC sample and the inferior resolution of the kinematic reconstruction of the h method compared with the $e\Sigma$ method used for NC events. The bins which are used in this measurement have to satisfy two quality criteria which have been studied with the simulation: their stability and purity[5] are required to be larger than 30%.

The reliability of the cross-section measurements is checked by comparing the results obtained from different kinematic reconstruction methods. Fig. 6a shows that there is good agreement between the measurements of $\tilde{\sigma}_{NC}$ with the e and the $e\Sigma$ methods in the region where the e method is precise ($y \gtrsim 0.1$). Good agreement is also found between the $e\Sigma$, the Σ and the DA methods (not shown) over the whole y range. Fig. 6b shows the NC reduced cross-section in

[5]The stability (purity) is defined as the number of simulated events which originate from a bin and which are reconstructed in it, divided by the number of generated (reconstructed) events in that bin.